JOURNAL OF GEOPHYSICAL RESEARCH: ATMOSPHERES, VOL. 118, 6738–6749, doi:10.1002/jgrd.50495, 2013

Probing into the impact of 3DVAR assimilation of surface PM_{10} observations over China using process analysis

Ziqiang Jiang,[1,2] Zhiquan Liu,[2] Tijian Wang,[1] Craig S. Schwartz,[2] Hui-Chuan Lin,[2] and Fei Jiang[3]

Received 15 January 2013; revised 9 May 2013; accepted 13 May 2013; published 17 June 2013.

[1] The capability of assimilating surface PM_{10} (particulate matter with diameters less than 10 μm) observations has been developed within the National Centers for Environmental Prediction Gridpoint Statistical Interpolation three-dimensional variational (3DVAR) data assimilation (DA) system. It provides aerosol analyses for the Goddard Chemistry Aerosol Radiation and Transport aerosol scheme within the Weather Research and Forecasting/Chemistry model. Control and assimilation experiments were performed for June 2011 over China to explore in detail the impact of assimilating surface PM_{10}. In the assimilation experiment, analyses were produced every 6 h to adjust the mass concentrations of different aerosol species. The statistical results from two parallel experiments demonstrate that the assimilation of surface PM_{10} observations can significantly reduce the uncertainty of initial aerosol fields and effectively improve the subsequent aerosol forecasts for at least 12 h. However, the benefit from the assimilation of PM_{10} diminishes rapidly with forecast range. Process analysis for PM_{10} formation indicates that the rapidly diminishing DA impact on aerosol forecasts, especially in early forecast hours, was dominated by vertical mixing with an additional contribution from advection. Both processes were mainly related to unbalanced aerosol fields in the horizontal and vertical after assimilating surface observations. These findings illustrate the importance of adjusting aerosol emission rates and the initial aerosol vertical profile.

Citation: Jiang, Z., Z. Liu, T. Wang, C. S. Schwartz, H.-C. Lin, and F. Jiang (2013), Probing into the impact of 3DVAR assimilation of surface PM_{10} observations over China using process analysis, *J. Geophys. Res. Atmos.*, *118*, 6738–6749, doi:10.1002/jgrd.50495.

1. Introduction

[2] Considerable progress has been made in recent years to reduce large uncertainties involved with numerical prediction of atmospheric aerosols [e.g., *Hakami et al*., 2005; *Henze et al*., 2007, 2009; *Yumimoto et al*., 2007, 2008a, 2008b; *Dubovik et al*., 2008; *Benedetti et al*., 2009; *Pagowski et al*., 2010; *Pagowski and Grell*, 2012; *Liu et al*., 2011; *Schwartz et al*., 2012]. These uncertainties can usually be attributed to inaccurate aerosol emissions and initial conditions (ICs) and deficiencies in the modeling system (e.g., nonlinear physical processes such as advection, diffusion, radiative effects, and cloud and precipitation formation). Data assimilation (DA), as a method to improve the model ICs, has been widely applied to operations and research in numerical weather prediction [e.g., *Parrish and Derber*, 1992; *Lorenc et al*., 2000; *Rabier et al*., 2000; *Gauthier et al*., 2007; *Kalnay*, 2010] for decades.

[3] However, aerosol DA remains in its infancy. Similar to meteorological DA, a variety of algorithms such as optimal interpolation (OI), two-dimensional variational (2DVAR), three-dimensional variational (3DVAR), four-dimensional variational (4DVAR), and ensemble Kalman filter (EnKF) DA techniques have been used in aerosol DA. Several attempts have recently been made to assimilate aerosol observations into numerical models with the purpose to improve the ICs. However, most of them have focused on assimilating satellite-derived aerosol products, due to their global coverage, especially aerosol optical depth (AOD) (e.g., OI [*Collins et al*., 2001; *Yu et al*., 2003; *Generoso et al*., 2007; *Adhikary et al*., 2008], Newtonian-nudging [*Wang et al*., 2004], 2DVAR [*Zhang et al*., 2008; *Schroedter-Homscheidt et al*., 2010], 3DVAR [*Liu et al*., 2011; *Schwartz et al*., 2012], and 4DVAR [*Benedetti et al*., 2009]). For instance, *Liu et al*. [2011] developed a 3DVAR algorithm to assimilate AOD retrievals from Moderate Resolution Imaging Spectroradiometer (MODIS) sensors while studying a dust storm in East Asia.

[4] Comparatively less work has been done to assimilate surface aerosol observations into ICs. *Lin et al*. [2008a] assimilated surface PM_{10} (particulate matter with diameters

[1]School of Atmospheric Sciences, Nanjing University, Nanjing, China.
[2]National Center for Atmospheric Research, Boulder, Colorado, USA.
[3]International Institute for Earth System Science, Nanjing University, Nanjing, China.

Corresponding author: Z. Liu, National Center for Atmospheric Research, Boulder, CO 80301, USA. (liuz@ucar.edu)

2169-897X/13/10.1002/jgrd.50495

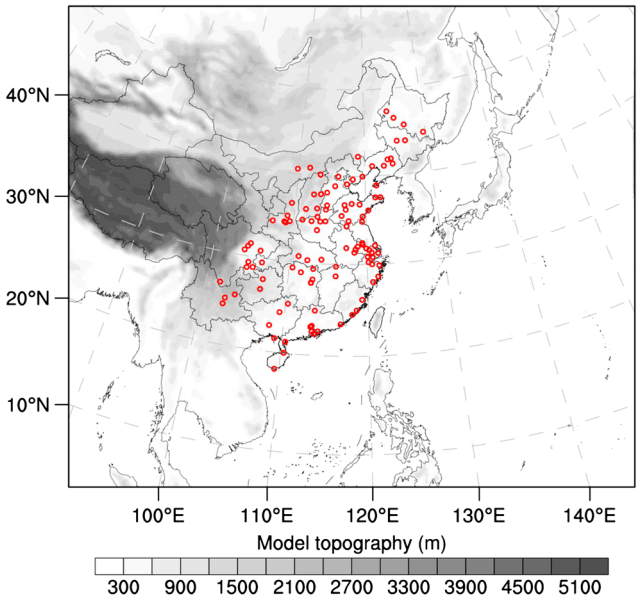

Figure 1. The model domain and the observation network with model topography (m). The open circles depict locations of measurement sites used for PM_{10} assimilation cycles and PM_{10} forecast verification.

less than 10 μm) observations in North China with an EnKF. Using the OI method, *Tombette et al*. [2009] assimilated surface PM_{10} over Europe and *Lee et al*. [2013] assimilated PM_{10} over South Korea. *Pagowski et al*. [2010] applied a 3DVAR approach to assimilate surface $PM_{2.5}$ (particulate matter with diameters less than 2.5 μm) observations over the continental United States (CONUS), and *Pagowski and Grell* [2012] used an EnKF for $PM_{2.5}$ DA over the CONUS. Moreover, both MODIS AOD and surface $PM_{2.5}$ observations were assimilated separately and together over the CONUS to illustrate the synergistic effect of assimilating different aerosol observations on aerosol forecasts [*Schwartz et al*., 2012]. These studies mostly demonstrated that along with successful DA of aerosol-related observations from both ground networks and satellite platforms, the adjusted aerosol ICs substantially improved subsequent aerosol forecasts at short ranges (~1–2 day) but not at extended periods. Also, when solely assimilating surface particulate matter observations, the DA impact on aerosol forecasts fades very quickly in the early forecast hours [*Tombette et al*., 2009; *Pagowski et al*., 2010; *Schwartz et al*., 2012; *Lee et al*., 2013].

[5] However, the studies mentioned above did not provide quantitative explanations regarding the rapidly diminishing DA impact of surface aerosol observations. Process analysis (PA) [e.g., *Jeffries and Tonnesen*, 1994; *Jang et al*., 1995; *Tonnesen*, 1995, *Tonnesen and Dennis*, 2000a, 2000b; *Jiang et al*., 2003; *Huang et al*., 2005; *Zhang et al*., 2009b; *Liu et al*., 2010], a mass balance analysis technique, may identify the main sources contributing to the rapidly diminishing DA impact by providing quantitative information on the formation mechanisms of gaseous and PM pollutants from various chemical and physical processes. Fewer PA studies have been undertaken that examine the formation of PM pollutants compared to those of gaseous pollutants. Previous studies [e.g., *Zhang et al*., 2009b; *Liu et al*., 2010] indicated that emissions, horizontal transport (including horizontal advection and diffusion), aerosol processes (e.g., gas-to-particle conversion processes), and cloud processes contribute the most to PM production and removal in the atmospheric boundary layer. However, at most surface sites, emission processes and vertical transport (including vertical advection and diffusion) are the predominant contributors to PM accumulation and loss. The contribution from dry deposition is relatively small.

[6] An aerosol 3DVAR DA framework has been developed by *Liu et al*. [2011] (hereafter L11) within the National Centers for Environmental Prediction (NCEP) Gridpoint Statistical Interpolation (GSI) 3DVAR DA system [*Wu et al*., 2002; *Kleist et al*., 2009], coupled to the Goddard Chemistry Aerosol Radiation and Transport (GOCART) aerosol scheme [*Chin et al*., 2000, 2002; *Ginoux et al*., 2001] within the Weather Research and Forecasting/Chemistry (WRF/Chem) model [*Grell et al*., 2005]. L11 first implemented MODIS AOD DA and applied it to a dust storm event over East Asia. *Schwartz et al*. [2012] (hereafter S12) further extended the system to allow the simultaneous assimilation of both MODIS AOD and surface $PM_{2.5}$. In this study, surface PM_{10} assimilation capability is implemented within the same framework. To the author's knowledge, this is the first attempt to assimilate the hourly ground-based PM_{10} observations within a 3DVAR DA system. Furthermore, PA capability for PM_{10} is also added into WRF/Chem to better understand the mechanisms of the fast-fading DA impact on aerosol forecasts.

[7] The next section provides a brief description of the WRF/Chem model and GSI DA system. The technical implementation of PM_{10} DA in the GSI 3DVAR system is given in section 3. The experimental design is described in section 4. The impact of PM_{10} DA and PA is detailed in section 5 before concluding in section 6.

2. Modeling and DA Systems

[8] The modeling and DA systems used here were described by L11 and S12. Therefore, generally brief descriptions follow, and important differences are noted.

2.1. WRF/Chem Model Configurations

[9] In this study, version 3.3.1 of the WRF/Chem model [*Grell et al*., 2005] was used to simultaneously predict weather and atmospheric composition. WRF/Chem is an "online" model, as its chemical and meteorological components are fully coupled. Same as L11 and S12, GOCART was chosen as the aerosol option. The original GOCART simulates 14 tropospheric aerosol types including sulfate,

Table 1. Statistics Comparing the Lowest Model Level PM_{10} Mass Concentrations From the Control and Assimilation Experiments, Calculated Against Observations From the MEP Network Over All 0000 and 1200 UTC Analyses During 01 to 28 June 2011

Exp. Name	Analyses Time (UTC)	Mean Obs. ($\mu g/m^3$)	Mean Sim. ($\mu g/m^3$)	BIAS ($\mu g/m^3$)	RMSE ($\mu g/m^3$)	CORR
Control	0000	77.16	54.66	−22.50	52.94	0.414
	1200	68.88	83.68	14.80	54.70	0.395
Assimilation	0000	77.16	69.31	−7.84	21.32	0.944
	1200	68.88	71.30	2.43	21.19	0.887

organic carbon (OC), black carbon (BC), mineral dust in five particle-size bins (effective radii of 0.5, 1.4, 2.4, 4.5, and 8.0 μm), and sea salt in four particle-size bins (effective radii of 0.3, 1.0, 3.25, and 7.5 μm for dry air). For OC and BC, hydrophobic and hydrophilic components are considered. However, for the GOCART module built in WRF/Chem, two additional variables "p25" and "p10" are also included to account for fine (effective diameter < 2.5 μm) and coarse (effective diameter $2.5 \sim 10$ μm) mode unspeciated aerosols. Model-output PM_{10} is diagnosed from 14 of 16 prognostic aerosol variables (see section 3).

[10] The model configurations mostly follow L11 for the model domain (Figure 1), grid spacing (27 km), horizontal grid points (261×222), vertical levels (45, with the model top at 50 hPa), physical parameterizations, and chemistry suite. Aerosol direct effects are allowed through the coupling between GOCART and the Goddard shortwave radiation scheme [*Fast et al*., 2006; *Barnard et al*., 2010]. Anthropogenic emissions were supplied offline from an Asia emissions inventory [*Streets et al*., 2003; *Zhang et al*., 2009a], and biogenic emissions were calculated online from the U.S. Geological Survey land use classification by using the Guenther scheme [*Guenther et al*., 1994; *Simpson et al*., 1995]. In addition, dust emissions [*Ginoux et al*., 2001], dimethylsulfide, and sea salt emissions [*Chin et al*., 2000, 2002] were also computed online. Lateral boundary conditions (LBCs) and ICs for meteorological fields were provided by the NCEP Global Forecast System (GFS). Aerosol and chemical ICs originated from previous WRF/Chem forecasts and chemical and aerosol LBCs are based upon an idealized, northern hemispheric, midlatitude, clean environmental vertical profile from the NOAA Aeronomy Lab Regional Oxidant Model [*McKeen et al*., 1991; *Liu et al*., 1996].

2.2. Incorporation of PA Within WRF/Chem

[11] To determine the roles of individual physical and chemical processes in species formation, PA has been widely applied to separate rates of change of species' concentrations into various contribution terms. The WRF/Chem model adopts the K-theory form of the scalar conservation equation to describe the tendency due to each process, given by

$$\frac{\partial C_i}{\partial t} = -\left[u\frac{\partial C_i}{\partial x} + v\frac{\partial C_i}{\partial y} + w\frac{\partial C_i}{\partial z}\right] + \frac{\partial}{\partial z}\left(K_e\frac{\partial C_i}{\partial z}\right) + D + R + E, \quad (1)$$

where the term on the left side is the concentration (C) tendency of species i with respect to time; the first term on the right-hand side represents horizontal and vertical advections in the x, y, and z directions, and u, v, and w are the mean wind speeds in the three directions, respectively; the second term denotes the vertical turbulent diffusion process (the horizontal diffusion terms are neglected), and K_e is turbulent diffusivities; the latter three terms are dry deposition (D), net chemical reactions (R), and source emission rate (E), respectively.

[12] We incorporated the PA capability within WRF/Chem by modifying the model source code to diagnose the tendency of each species concentration due to each process every time step by differencing species' concentrations before and after each process. The accumulated tendency, integrated during a period of time in each grid cell, is commonly referred to as the integrated process rate (IPR) [*Huang et al*., 2005; *Zhang et al*., 2009b; *Liu et al*., 2010]. In this paper, the PM_{10} IPR is examined every hour to explore the relative contributions of major atmospheric processes in PM_{10} formation. Positive values of IPR indicate PM_{10} production from various processes, and negative values indicate PM_{10} losses. Thus, the contribution of each process may be compared directly between parallel experiments, especially for the near-surface layer, to further examine the DA impact on subsequent WRF/Chem aerosol forecasts.

2.3. GSI 3DVAR System

[13] The GSI 3DVAR DA system produces an analysis in model grid space. The analysis is obtained through the minimization of a scalar objective function J(**x**) given by

$$J(\mathbf{x}) = \frac{1}{2}(\mathbf{x}-\mathbf{x_b})^{\mathrm{T}}\mathbf{B}^{-1}(\mathbf{x}-\mathbf{x_b}) + \frac{1}{2}[H(\mathbf{x})-\mathbf{y}]^{\mathrm{T}}\mathbf{R}^{-1}[H(\mathbf{x})-\mathbf{y}], \quad (2)$$

where **x** is the model state and the subscript b denotes the background state, **y** is the observation vector, H is the observation operator that computes the observation estimates from the model state vector, **B** denotes the background error covariance (BEC) matrix, and **R** represents the observation error covariance matrix, including contributions from measurement and representativeness errors (see section 3.2 for details). The error covariance matrices determine the relative contributions of the background and observation terms to the final analysis.

[14] In our case, GSI was used to assimilate surface PM_{10} observations without meteorological DA. Similar to L11 and S12, the 3-D mass mixing ratios of the 16 GOCART aerosol species at each grid point comprised the analysis (or control) variables in the GSI 3DVAR minimization procedure. This speciated approach to aerosol DA was introduced by L11 and further applied by S12. Different from L11 and S12, an additional variable P_{10} (coarse-mode unspeciated aerosols) was introduced into the analysis vector here as it is an important contributor to PM_{10}. However, a total of 14 control variables were used to diagnose the model estimate PM_{10} at the observation locations within the GSI 3DVAR system, as detailed in section 3. Thus, only 14 GOCART aerosol variables were updated in the aerosol DA.

[15] As in L11 and S12, the latitude-dependent BEC statistics for each aerosol species were estimated using the National Meteorological Center (now known as NCEP) method [*Parrish and Derber*, 1992; *Rabier et al*., 1998], which takes differences between forecasts of different lengths valid at common times. Utilizing the differences of 24 and 12 h WRF/Chem forecasts of the analysis variables valid at the same time for 59 pairs valid at either 0000 and 1200 UTC over the experimental period (June 2011), standard deviations and horizontal and vertical length scales for each aerosol species' BEC were calculated. No cross correlation between different aerosol species was considered because of the incapability of the current GSI 3DVAR to directly model the cross correlations in the B matrix. Work is underway to take into account cross correlation between species through the ensemble-based DA techniques [*Pagowski and Grell*, 2012].

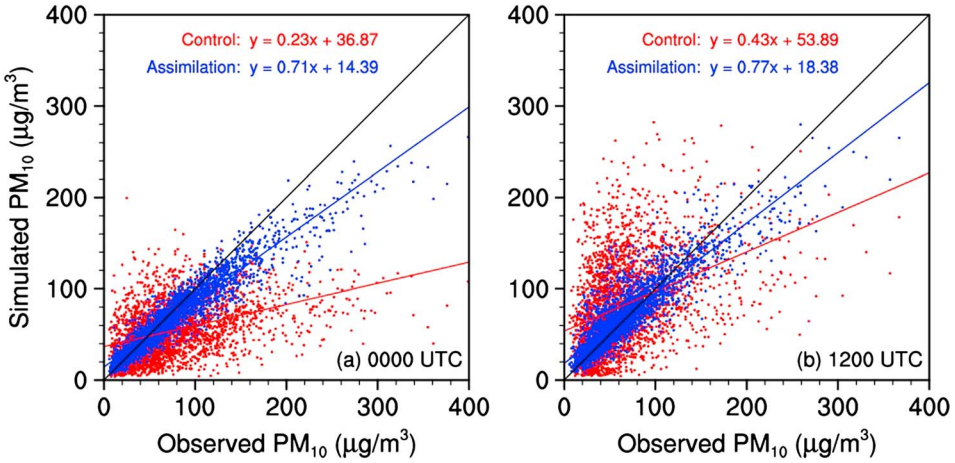

Figure 2. Scatter plots of simulated versus observed PM_{10} mass concentrations over all (a) 0000 and (b) 1200 UTC initializations from the control (red) and assimilation (blue) experiments.

3. Implementation of PM_{10} DA

3.1. PM_{10} Observation Operator

[16] To assimilate PM_{10}, it was necessary to derive model-simulated PM_{10} at the observation locations. Following the WRF/Chem GOCART aerosol module, the diagnostic variable PM_{10} is obtained from the 14 of 16 aerosol species, mineral dust and sea salt in the largest particle-size bins were excluded. To assimilate a surface PM_{10} observation, a model estimate of PM_{10} is diagnosed at the lowest vertical level by summing mass mixing ratios of aerosol particles, given as

$$PM_{10} = \rho_d[(P_1 + P_2) + (D_1 + D_2 + D_3 + 0.87D_4) + 1.8(O_1 + O_2) + (B_1 + B_2) + (S_1 + S_2 + S_3) + 1.375U], \quad (3)$$

where P_1 and P_2 represent fine- and coarse-mode unspeciated aerosol contributions to PM_{10}, respectively; D_1, D_2, and D_3 (S_1, S_2, and S_3) are mineral dust (sea salt) aerosols in three smallest particle-size bins, and D_4 denotes mineral dust in the fourth smallest particle-size bin (effective radius of 4.5 μm); O_1 and O_2 (B_1 and B_2) are hydrophobic and hydrophilic OC (BC), respectively; and U denotes sulfate. Similar to S12, coefficients <1 in equation (3) account for the 10 μm diameter cutoff of GOCART aerosols for PM_{10}, and coefficients >1 empirically account for additional fine particulate mass not predicted explicitly by GOCART, such as oxygen contained in organic aerosols (associated with OC) and ammonium (typically associated with sulfate aerosols). The dry air density ρ_d converts the units from μg/kg to μg/m^3 for consistency with the observations. Before equation (3) is applied within GSI, the aerosol analysis variables and ρ_d are bilinearly interpolated in the horizontal to the observation locations. Since altitudes of some measurement sites are not available, differences between model topography and reality were neglected, and no vertical extrapolation was performed. Observations taken within 1 h of the analysis were assimilated.

3.2. PM_{10} Observation Data and Errors

[17] Hourly averaged surface PM_{10} concentrations for June 2011 were obtained from the Ministry of Environmental Protection (MEP) of China. At each measurement site, the samplings are heated to measure the mass of dry particulate

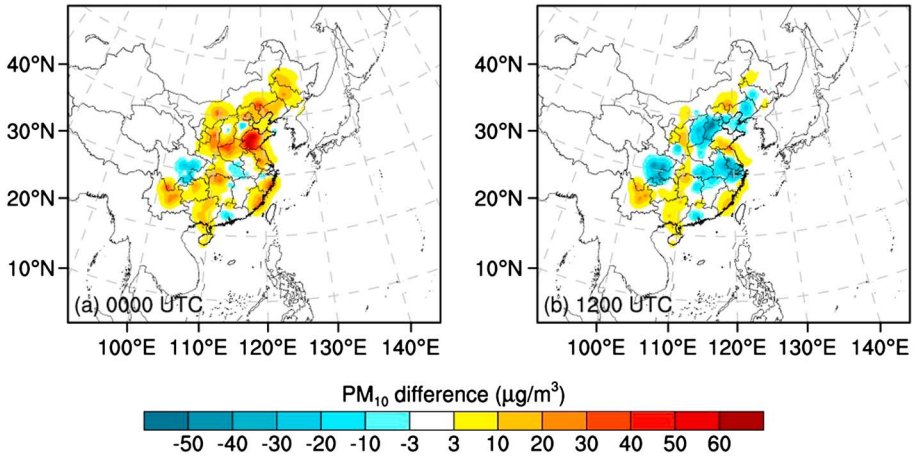

Figure 3. PM10 mass differences (assimilation minus control) at the lowest model level averaged over all (a) 0000 and (b) 1200 UTC initializations.

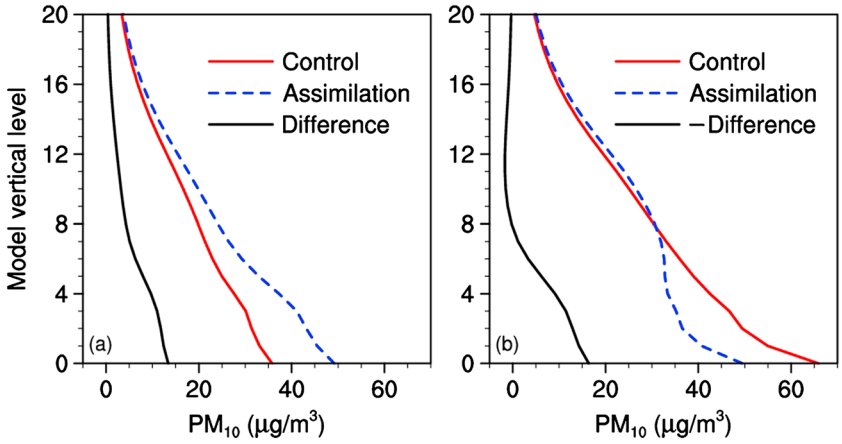

Figure 4. Vertical profiles of simulated PM10 mass concentrations from the control (red) and assimilation (blue) experiments, and the difference (black), averaged over all 0000 and 1200 UTC initializations for locations where there are (a) positive and (b) negative differences at the lowest model level. Note that the legend in Figure 4a differs partly from that of Figure 4b.

matter using the tapered element oscillating microbalance (TEOM) method [*Green et al*., 2001; *Charron et al*., 2003]. Figure 1 shows the locations of 112 measurement sites used for the PM_{10} assimilation experiment and forecast verification. Observation sites span most of central and eastern China and are primarily located in urban and suburban areas.

[18] MEP PM_{10} data were provided without information regarding data quality. To ensure data reliability before DA, PM_{10} observations were subject to quality control (QC). Two QC checks were performed, including value-range and time-continuity checks. First, PM_{10} observational values that fell outside of subjectively chosen lower (6 μg/m^3) and upper (425 μg/m^3) limits were deemed unrealistic and rejected. Second, time continuity was checked to eliminate gross outliers. Similar to the "buddy check" used in meteorological DA [e.g., *Dee et al*., 2001], any measurement $O(t)$ will pass

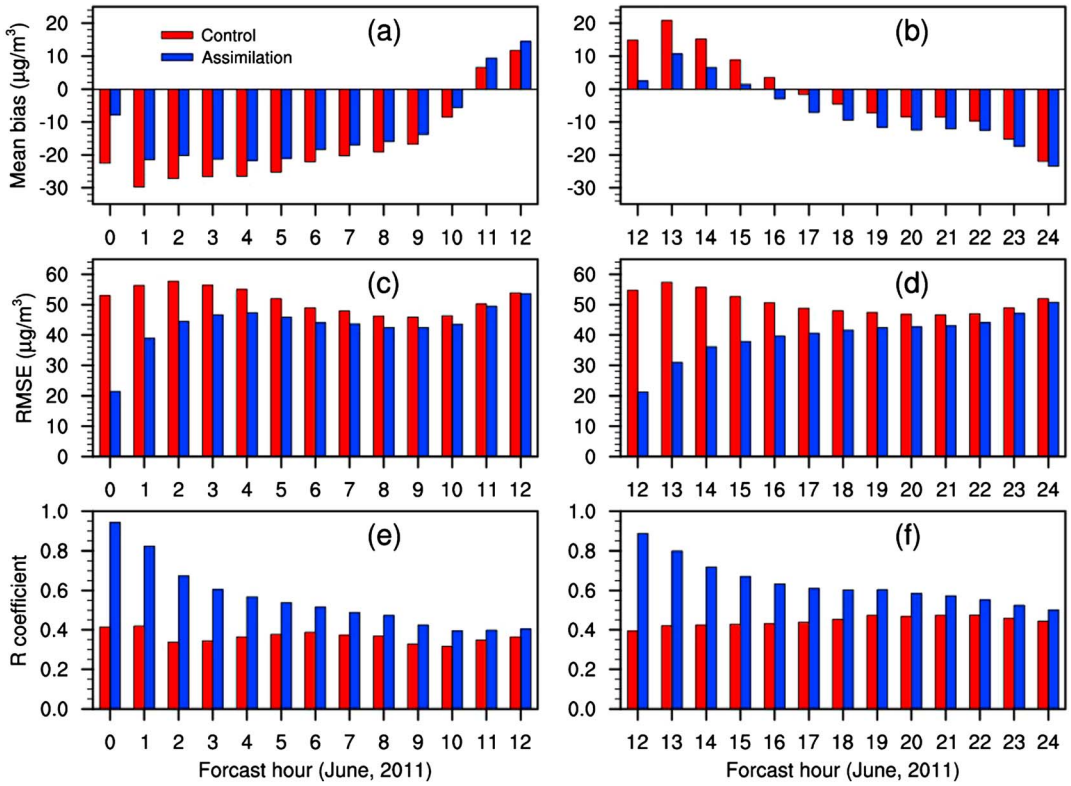

Figure 5. Evaluation statistics of surface PM_{10} forecasts as a function of forecast range calculated against observations: (top) mean bias (μg/m^3), (middle) root-mean-square error (μg/m^3), and (bottom) correlation coefficient. The forecasts are produced from the 0000 (left) and 1200 (right) UTC initializations during 1 to 28 June 2011.

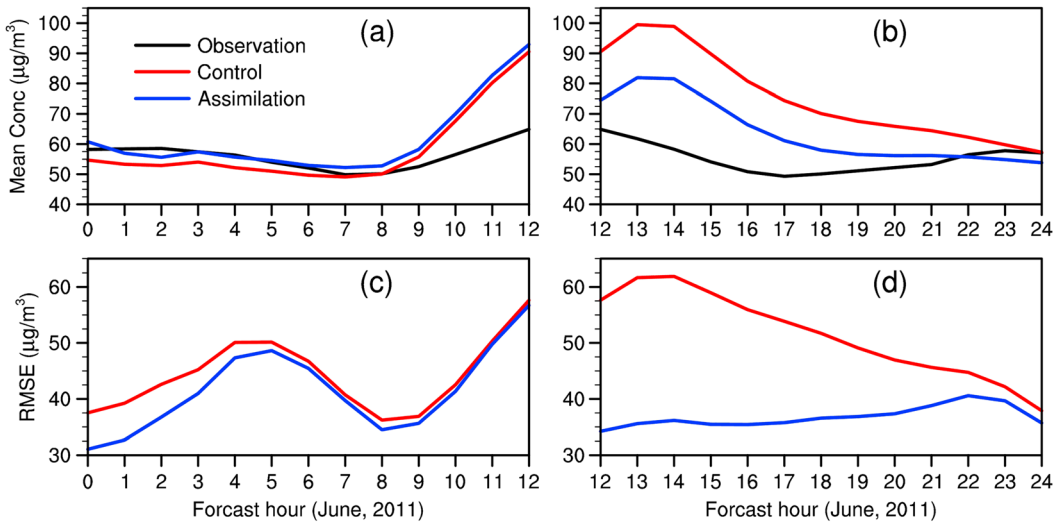

Figure 6. (top) Mean concentration (μg/m^3) and (bottom) root-mean-square error (μg/m^3) of surface $PM_{21.5}$ forecasts as a function of forecast range, verified against observations from Nanjing and Shanghai during 1 to 28 June 2011. The forecasts are produced from the 0000 (left) and 1200 (right) UTC initializations.

the time-continuity check if it satisfies $|O(t) - O(t \pm 1)| \leq m(t)$, where the function $m(t)$ is determined empirically (e.g., $m(t) = 50 + 0.15O(t)$ for this study).

[19] As mentioned in section 2.3, the observation error covariance matrix **R** in equation (1) contains both measurement and representativeness errors. However, observation errors are not provided with observations, and no general formulation is available to estimate such errors. Similar to S12, the measurement error ε_o is defined as $\varepsilon_o = 1.5 + 0.0075 * \Pi_o$, where Π_o denotes PM_{10} observational values (units: μg/m^3). Thus, higher PM_{10} values were associated with larger measurement errors. The representativeness error, also following *Elbern et al*. [2007] and S12, depended on the model resolution and the characteristics of the observation locations. The observation errors are assumed uncorrelated so that **R** is a diagonal matrix.

4. Experimental Design

[20] Two parallel experiments were performed to evaluate the impact of PM_{10} DA on analyses and forecasts of aerosols over China. One experiment served as the control and did not employ any DA, while PM_{10} DA was implemented in the other. Both experiments began from the same set of ICs valid at 0000 UTC 01 June 2011 that were spun-up over 5 days beginning 27 May, similar to *Pagowski et al*. [2010] and S12. Each experiment initialized a new WRF/Chem forecast every 6 h between 0000 UTC 01 June and 0000 UTC 28 June 2011. All 0000 and 1200 UTC initializations produced 12 h forecasts, while 6 h forecasts were produced from the 0600 and 1800 UTC initializations. Each initialization, both LBCs and ICs for meteorological fields were updated by interpolating GFS analyses onto the model domain, and gaseous chemical variables were initialized from the previous cycle's 6 h forecast.

[21] As described by L11 and S12, both experiments only differed regarding initialization of the 16 GOCART aerosol species contained in the GSI analysis. In the control experiment, the initial GOCART aerosol fields were simply taken from the previous cycle's 6 h forecast. However, the PM_{10} assimilation experiment implemented a 3DVAR aerosol analysis every 6 h, using the GOCART aerosol fields from the previous cycle's 6 h forecast as the background. The analyses were then used as aerosol ICs for subsequent WRF/Chem forecasts. Thus, the experiments only differed in that 3DVAR DA updated the GOCART aerosol species in one experiment but not the other. Both experiments used the same physical and chemistry options outlined in section 2.1.

[22] The analyses and forecasts from the two experiments were compared to surface PM_{10} measurements. The results of these comparisons are now described.

5. Results

[23] This section presents results from the control and assimilation experiments outlined above. Since surface PM_{10} DA had a very small impact on AOD (not shown), we only performed verification against MEP PM_{10} data and surface $PM_{2.5}$ observations from two sites in Nanjing and Shanghai. Although forecasts were produced every 6 h, we focus on examining the PM_{10} DA impact on aerosol ICs at 0000 and 1200 UTC (local time = UTC + 8 h) before evaluating the subsequent WRF/Chem forecasts and then discuss the IPR differences in PM_{10} formation. Here, three basic statistical measures, mean bias (BIAS), root-mean-square error (RMSE), and correlation coefficient (CORR), as described in *Zhang et al*. [2006], are applied to evaluate the results. When compared with surface PM_{10} and $PM_{2.5}$ observations, the model values at the lowest vertical level were horizontally interpolated to the observation sites.

5.1. Impacts on Aerosol ICs

[24] The model evaluation statistics (Table 1) from the control and assimilation experiment for the lowest model level PM_{10} mass concentrations were calculated against observations from the MEP network over all 0000 and 1200

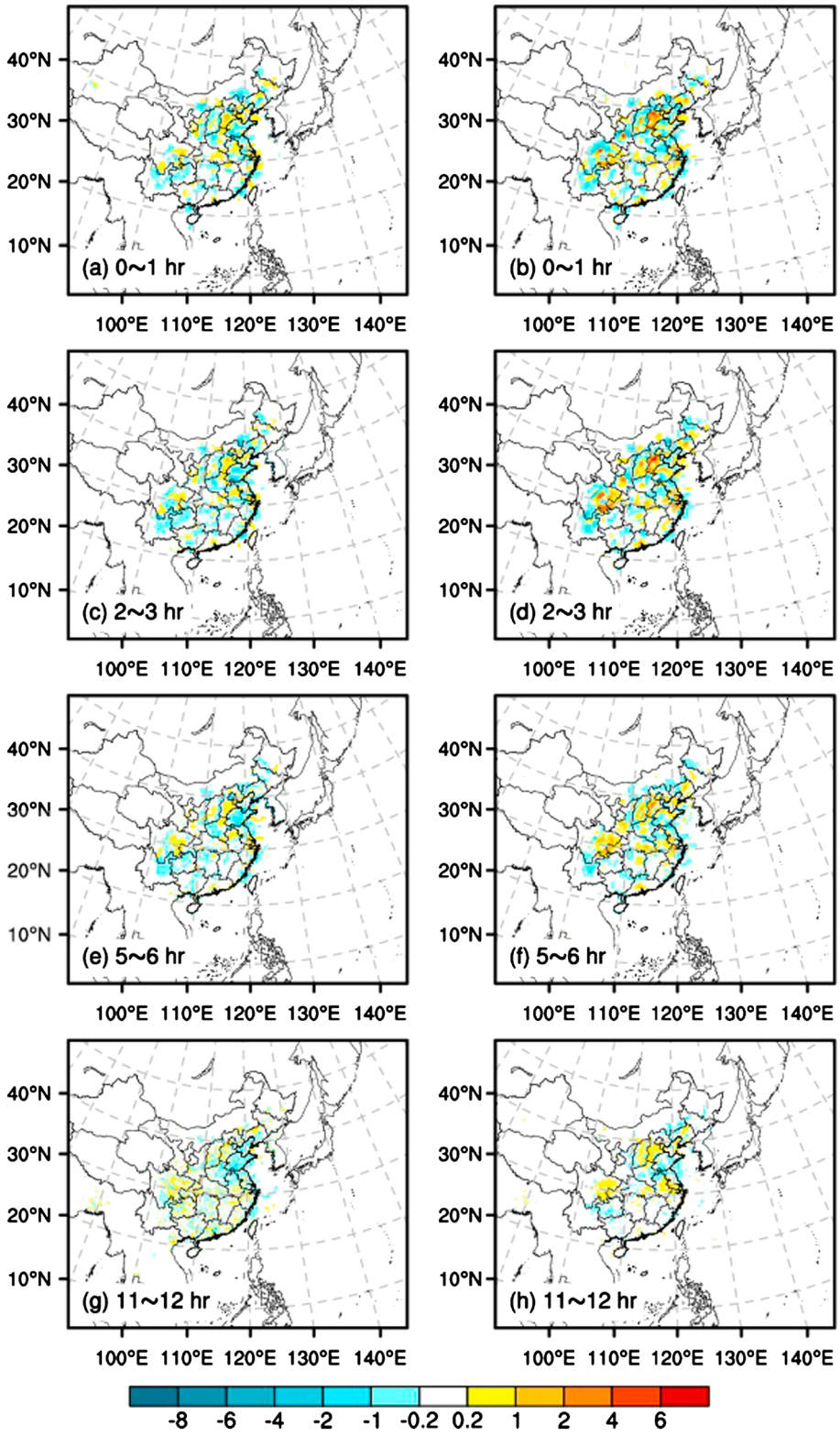

Figure 7. Spatial distribution of average differences of hourly PM_{10} IPRs ($\mu g/m^3/h$) between the two experiments (assimilation minus control) advection processes (horizontal and vertical) at the lowest model level, aggregated over all 0000 (left) and 1200 (right) UTC initializations.

UTC initializations during 01 to 28 June 2011. There are significant systematic biases and large RMSEs for the control. The negative model bias of -22.5 $\mu g/m^3$ at 0000 UTC (morning) indicates a significant underestimation, about 29.1% lower than the observed PM_{10} concentrations. Conversely, a positive bias of 14.8 $\mu g/m^3$ at 1200 UTC (evening) indicates a significant overestimation, about 21.5% higher than the observed PM_{10} values. Additionally, the

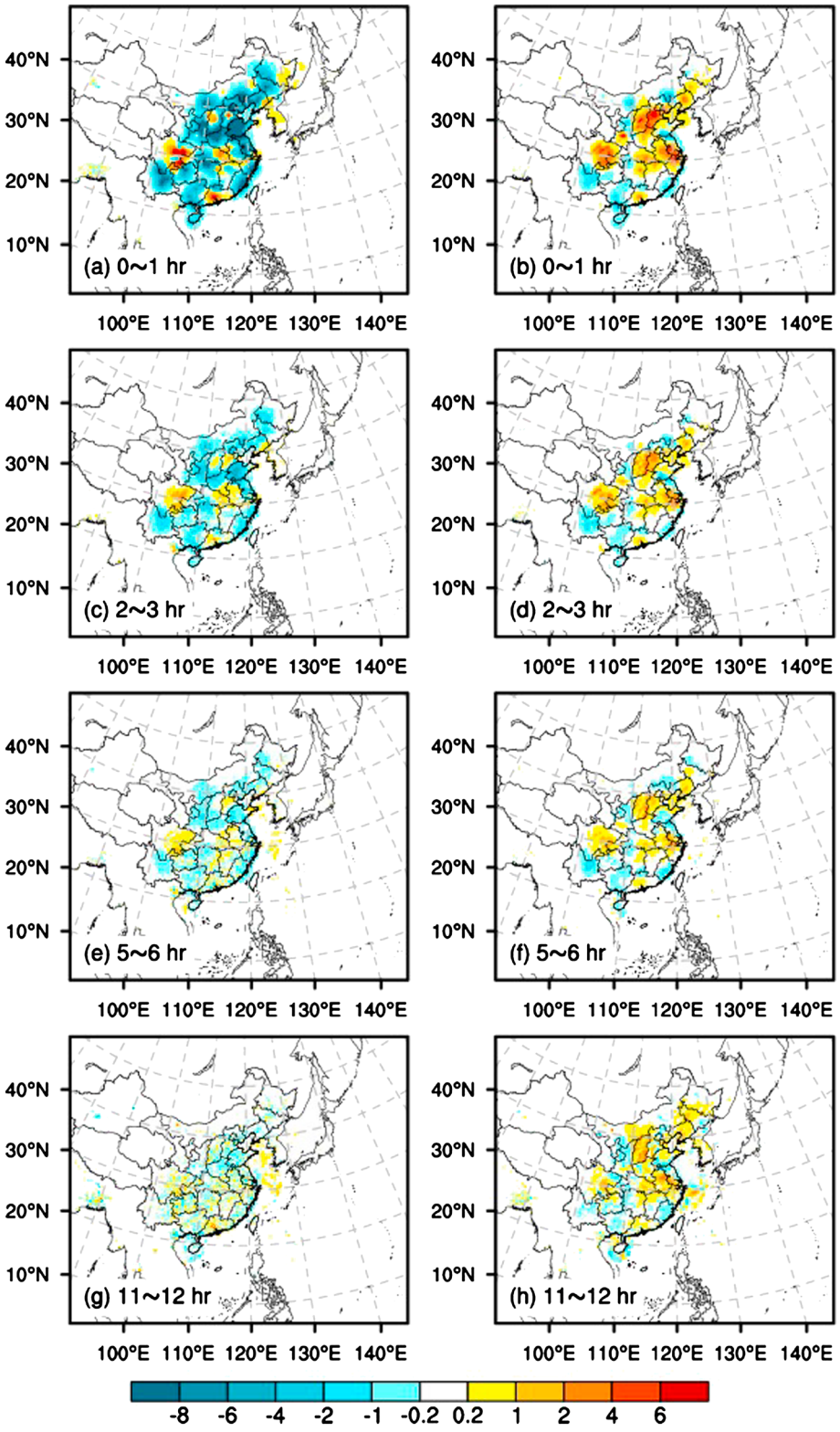

Figure 8. Same as Figure 7 except for vertical diffusion processes.

mean RMSE and CORR between the control and the observations is about 53.8 μg/m^3 and 0.4, respectively. These magnitudes are similar to those of PM_{10} forecast error statistics over the Yangtze River Delta region [*Wang et al.*, 2012] and the Pearl River Delta region [*Chen et al.*, 2009].

[25] After assimilating surface PM_{10} observations, the statistics show much better agreement with observations than the control. Overall biases are dramatically reduced; RMSEs are decreased by about 60%, and CORRs are greatly increased from about 0.4 to 0.9. Scatter plots of simulated

PM_{10} mass concentrations over all 0000 and 1200 UTC initializations from the control and assimilation experiments against observations are also illustrated in Figure 2. These results indicate that initial PM_{10} fields can be adjusted effectively by our DA approach.

[26] Figure 3 depicts the spatial distribution of time-averaged PM_{10} differences (assimilation minus control) at the lowest model level over all 0000 and 1200 UTC initializations. The patterns closely match the measurement sites in Figure 1. Consistent with Table 1, at 0000 UTC, the positive differences indicate PM_{10} DA primarily increased the model PM_{10}, and the largest value (greater than 60 $\mu g/m^3$) occurs in Shandong province (Figure 3a). At 1200 UTC, the negative differences indicate PM_{10} DA primarily decreased the model PM_{10}, and the lowest value (less than -50 $\mu g/m^3$) appears in South Hebei province (Figure 3b). The differences imply model errors were present, likely from inaccurate emission rates in time and space. For instance, some underestimation may come from crop residue burning due to summer harvest [*Yang et al*., 2008], not properly represented in the emissions.

[27] The vertical profiles of simulated PM_{10} mass concentrations from the control and assimilation experiments are given in Figure 4 separately for locations where the surface PM_{10} differences were positive and negative. The extent of the vertical impact of PM_{10} DA is mainly determined by the vertical correlation of BECs [*Benedetti and Fisher*, 2007]. Although the DA impact extended up to model level 18, ~3.2 km above ground level (AGL), the biggest impact was confined below model level 8 (~0.8 km AGL). The change of total aerosol mass due to PM_{10} DA diminished rapidly as a function of height, which is consistent with S12.

[28] It is also interesting to examine how DA impacted the PM_{10} vertical gradients below 1 km. Where aerosol mass was increased by PM_{10} DA, the vertical gradient of difference was negative, indicating after DA vertical aerosol mass gradient became stronger (Figure 4a). Conversely, PM_{10} DA produced far weaker mass gradients in the vertical where aerosol mass decrease occurred (Figure 4b). These results show that PM_{10} DA greatly changed vertical structures of aerosol mass at near-surface model levels, which were also found by S12 when solely assimilating $PM_{2.5}$. Vertical gradient controls the vertical diffusion term in equation (1).

5.2. Forecast Verification

[29] To better understand the performance of the control and assimilation experiments, the BIAS, RMSE, and CORR of surface PM_{10} forecasts as a function of forecast range were calculated against MEP observations separately for the 0000 and 1200 UTC initializations.

[30] The control experiment had biases (~−30 to 20 $\mu g/m^3$) that were characterized by the diurnal cycle (Figures 5a and 5b). The positive (negative) biases spanned 1100 (1700) to 1600 (1000) UTC, indicating that WRF/Chem overpredicted (underpredicted) the surface PM_{10} in this time range. DA impact on systematic biases of aerosol forecasts depended greatly on sign of the initial and subsequent forecast biases from the control. Where the signs were same (opposite) between the initial and subsequent forecast biases, improvement (deterioration) on subsequent forecast biases was produced by PM_{10} DA. Both forecasts from 0000 and 1200 UTC initializations had the same behaviors, which were primarily driven by overall increase or decrease of model aerosol mass after DA.

[31] Even though the assimilation experiment had larger biases at times, PM_{10} DA produced consistently lower RMSEs and higher correlations for the entire 12 h forecasts, reflecting the overall benefit of assimilating surface PM_{10} observations (Figures 5c–5f). However, the differences between the experiments diminished with forecast lead time, likely due to model processes and emissions dominating at later periods [*Kahnert*, 2008]. Also, the forecast accuracy from the assimilation experiment decreased with time, as RMSEs increased and CORRs decreased. For instance, the relative RMSE reduction due to DA is 59.7% at 0000 UTC initialization and then decreases to 30.8%, 17.4%, 9.9%, and 0.5% for the first, third, sixth, and twelfth of forecasts, respectively (Figure 5c). Similarly, the relative correlation increase due to DA is 128.0% at 0000 UTC initialization and then decreases to 96.6%, 76.1%, 33.1%, and 11.5% for the corresponding forecast ranges (Figure 5e). *Tombette et al*. [2009] and *Lee et al*. [2013], who assimilated surface PM_{10} observations over Europe and South Korea, respectively, also noticed a small DA impact beyond about 12 h forecast.

[32] In addition, we also evaluated $PM_{2.5}$ forecasts at Nanjing and Shanghai (two megacities over Eastern China) for the whole experimental period. The model-simulated $PM_{2.5}$ was diagnosed within WRF/Chem, as described in S12, and the surface $PM_{2.5}$ mass concentration was measured using the TEOM method. Figure 6 shows statistics, as a function of forecast range, of mean $PM_{2.5}$ mass concentrations from observation, control, and PM_{10} DA experiments (top two panels) and RMSEs for the control and DA experiments verified against surface $PM_{2.5}$ observations (bottom two panels). As in Figure 5, statistics were calculated separately for 0000 (left) and 1200 (right) UTC initializations. These results are overall consistent with Figure 5, even though the error magnitudes and variation with forecast range differed slightly. The rapidly decreasing DA impact is also evident in $PM_{2.5}$ verification.

[33] This behavior of the short-lasting DA impact with the forecast lead time has also been found by *Tombette et al*. [2009] and *Lee et al*. [2013] when assimilating surface PM_{10} observations and *Pagowski et al*. [2010] and S12 when assimilating surface $PM_{2.5}$ data. S12 gave a qualitative discussion on this issue and concluded that advection and vertical mixing are the main causes for the lack of long-lasting surface observation impact. Likewise, *Elbern et al*. [2007] also remarked that optimizing the emission rate is far more important than improving ICs by assimilating surface ozone observations through the EnKF and 4DVAR approaches, indicating that the long-range forecast is much less sensitive to the initial state than the emissions. We implemented PA capability within the WRF/Chem model, which provides a method to quantify the contributions of various processes to PM_{10} formation from both experiments, as detailed in the next subsection.

5.3. PA for PM_{10} Formation

[34] As stated in section 2.2, while the IPR deals with the net effect of all the physical and chemistry processes on model simulation, the IPR differences between parallel experiments represent various process-contribution differences. The IPR diagnosed from the control experiment showed that

the emission process (vertical diffusion) was the predominant contributor to PM_{10} production (loss) at the lowest model level. Advection (including horizontal and vertical) and dry deposition only played secondary roles in PM_{10} formation, and the contribution from other processes (such as chemical reactions) was very small (not shown). These findings are consistent with *Chen et al*. [2009], *Zhang et al*. [2009b], and *Liu et al*. [2010], who examined the relative importance of major atmospheric processes in PM formation.

[35] In this study, the IPR differences, originated mainly from adjusted aerosol ICs due to PM_{10} DA, were examined to identify the main cause of the short-lasting DA impact of surface observations. Figure 7 depicts the time-averaged spatial distribution of PM_{10} IPR differences (assimilation minus control) of advection processes at the lowest model level for various forecast hours separately for 0000 and 1200 UTC initializations. The IPR differences have no significant change in the first three hours (up to ± 4 $\mu g/m^3/h$) and become smaller beyond the fifth forecast hour. Differences were mainly caused by localized increment structures around the measurement sites (Figure 3). The PM_{10} IPR differences of vertical diffusion process are also presented in Figure 8. The largest differences occur in the initial hour (up to -20 $\mu g/m^3/h$ on minimum and 8 $\mu g/m^3/h$ on maximum) and then are reduced dramatically and rapidly with forecast hour, more intense at day (0000 to 1200 UTC) than at night (1200 to 0000 UTC). Note that negative values indicate more loss or less production of PM_{10} in the assimilation experiment and vice versa. In particular, the negative (positive) differences for vertical mixing indicate the enhanced (reduced) upward diffusion from the ground or downward dilution from above.

[36] Compared to advection process, the differences of vertical mixing are larger in value and wider in area within the same time, dominating the IPR differences between the two experiments. Clearly, vertical diffusion was more important than advection, causing the rapidly diminishing DA impact. The IPR differences are relatively small for the other processes, and the time-averaged values are lower than ± 1.5 $\mu g/m^3/h$ for all forecast ranges (not shown).

[37] Recall that the same GFS analyses were used in both experiments for meteorological ICs. Therefore, initial aerosol fields primarily determine the strength of advection and diffusion processes. We note that a good spatial coherence is shown between PM_{10} mass differences and PM_{10} IPR differences of vertical mixing at the lowest model level, where positive (negative) surface PM_{10} differences mostly correspond to negative (positive) IPR differences (Figures 3 and 8). This further indicates that, where aerosol mass increase (decrease) occurred, enhanced (reduced) upward diffusion produces more dilution (accumulation) of surface aerosol mass. Thus, surface PM_{10} differences weaken continuously, leading to rapidly diminishing DA impact with time, especially in the early forecast hours.

[38] As evidenced in Figure 4, vertical gradients of aerosol mass at initializations were markedly changed after assimilating surface PM_{10} observations, also found by S12 when solely assimilating $PM_{2.5}$. Thus, whenever surface PM_{10} observations are assimilated, sharper (weaker) vertical gradient due to DA enhanced (lessen) vertical mixing and quickly diluted (accumulated) surface aerosol mass, leading to the fast-fading DA impact especially in the early forecast hours. Furthermore, *Tombette et al*. [2009], *Pagowski et al*. [2010], S12, and *Lee et al*. [2013] also noted that fast-fading DA impact was generated in the early forecast hours when assimilating surface PM observations. Conversely, L11 and S12 found that AOD DA refines the total aerosol mass throughout the column, maintaining similar vertical structures, which allows a longer-lasting DA impact. These results all underline the importance of a correct vertical profile of aerosol mass, implying some limitation of assimilating the surface observations into ICs.

6. Summary and Discussion

[39] The ability of assimilating hourly averaged surface PM_{10} observations from the MEP network was added into the aerosol DA framework within the GSI 3DVAR analysis system. This system was applied to daily aerosol forecasts produced in June 2011 over China. In the assimilation experiment, an aerosol analysis was performed every 6 h to update the WRF/Chem aerosol variables. To evaluate the effectiveness of DA, a control experiment without DA was also performed. Results revealed that aerosol analyses matched PM_{10} observations much better than the control, which improved the surface PM_{10} forecasts up to at least 12 h in terms of RMSE and correlation. However, the forecast bias can be enlarged by DA when its sign is opposite to that at initial time. Overall, our findings suggest that model-driven aerosol biases [e.g., *McKeen et al*., 2007; *Misenis and Zhang*, 2010; *Lin et al*., 2008b; *Zhang et al*., 2010] can be mitigated by aerosol DA. Further studies are needed to further document the processes leading to aerosol bias.

[40] As also found in earlier work, the DA impact diminished rapidly with forecast range when solely assimilating surface aerosol observations. PA was carried out within WRF/Chem to probe into the differences in PM_{10} formation between the control and assimilation experiments. The results show that fast-fading DA impact on aerosol forecast, especially in the early forecast hours, mostly came from vertical mixing, with minor contributions from horizontal and vertical advections. This behavior is mainly related to unbalanced aerosol fields in the horizontal and vertical after assimilating surface observations into the initial model state. This implies the need for aerosol observations with vertical information for more accurate 1–2 day forecast of surface aerosols.

[41] In the current assimilation experiment, only the initial state of aerosol fields was adjusted by cyclic PM_{10} DA, which limited the DA impact on long-range aerosol forecasts. There are some indications that emission sources appear to be the primary cause of the PM production [e.g., *Chen et al*., 2009; *Zhang et al*., 2009b; *Liu et al*., 2010], implying that emission adjustments are critical to the model forcing needed to maintain aerosol profile adjustments due to the assimilation of surface PM_{10} observations. As emission uncertainty is widely recognized as a major factor limiting the accuracy of aerosol forecasts, especially in areas with air quality problems [*Dubovik et al*., 2008], it should be particularly promising to analyze sources of aerosols and their precursors. Recently, adjoint inverse modeling systems [e.g., *Hakami et al*., 2005; *Elbern et al*., 2007; *Yumimoto et al*., 2007, 2008a; *Henze et al*., 2009; *Ku and Park*, 2011] have allowed

a "top-down" emission optimization at the model grid scale, providing constraints on emissions from surface aerosol observations. It can be expected that emission optimization will produce better forecast results than simply adjusting the initial model state by assimilating surface observations [e.g., *Henze et al*., 2009]. Furthermore, more desirable forecast improvements will likely be achieved by the joint adjustment of ICs and emission inventories. These issues will be addressed in future work.

[42] **Acknowledgments.** We are very grateful to the U. S. Air Force Weather Agency for partially funding this work. NCAR is sponsored by the National Science Foundation (NSF). This work was partly supported by National Key Basic Research Development Program of China (2011CB403406, 2010CB428503), the National Special Fund for the Weather Industry (GYHY201206011), and the Natural Science Foundation of Jiangsu Province (BK2010600). The Ministry of Environmental Protection of the People's Republic of China is also thanked for making their data available.

References

Adhikary, B., S. Kulkarni, A. Dallura, Y. Tang, T. Chai, L. R. Leung, Y. Qian, C. E. Chung, V. Ramanathan, and G. R. Carmichael (2008), A regional scale chemical transport modeling of Asian aerosols with data assimilation of AOD observations using optimal interpolation technique, *Atmos. Environ.*, *42*(37), 8600–8615, doi:10.1016/j.atmosenv.2008.08.031.

Barnard, J. C., J. D. Fast, G. Paredes-Miranda, W. P. Arnott, and A. Laskin (2010), Technical note: Evaluation of the WRF-Chem "Aerosol Chemical to Aerosol Optical Properties" module using data from the MILAGRO campaign, *Atmos. Chem. Phys.*, *10*, 7325–7340, doi:10.5194/acp-10-7325-2010.

Benedetti, A., and M. Fisher (2007), Background error statistics for aerosols, *Q. J. R. Meteorol. Soc.*, *133*(623), 391–405, doi:10.1002/qj.37.

Benedetti, A., et al. (2009), Aerosol analysis and forecast in the European Centre for Medium-Range Weather Forecasts Integrated Forecast System: 2. Data assimilation, *J. Geophys. Res.*, *114*, D13205, doi:10.1029/2008JD011115.

Charron, A., R. M. Harrison, S. Moorcroft, and J. Booker (2003), Quantitative interpretation of divergence between PM_{10} and $PM_{2.5}$ mass measurement by TEOM and gravimetric (Partisol) instruments, *Atmos. Environ.*, *38*, 415–423.

Chen, X., Y. Feng, J. Li, W. Lin, S. Fan, A. Wang, S. Fong, and H. Lin (2009), Numerical simulation on the effect of sea-land breezes on atmospheric haze over the Pearl River Delta region, *Environ. Model. Assess.*, *14*(3), 351–363.

Chin, M., R. B. Rood, S.-J. Lin, J.-F. Muller, and A. M. Thompson (2000), Atmospheric sulfur cycle simulated in the global model GOCART: Model description and global properties, *J. Geophys. Res.*, *105*, 24, 671–24,678.

Chin, M., P. Ginoux, S. Kinne, O. Torres, B. N. Holben, B. N. Duncan, R. V. Martin, J. A. Logan, A. Higurashi, and T. Nakajima (2002), Tropospheric aerosol optical thickness from the GOCART model and comparisons with satellite and Sun photometer measurements, *J. Atmos. Sci.*, *59*(3), 461–483.

Collins, W. D., P. J. Rasch, B. E. Eaton, B. V. Khattatov, J.-F. Lamarque, and C. S. Zender (2001), Simulating aerosols using a chemical transport model with assimilation of satellite aerosol retrievals: Methodology for INDOEX, *J. Geophys. Res.*, *106*, 7313–7336, doi:10.1029/2000JD900507.

Dee, D. P., L. Rukhovets, R. Todling, A. M. da Silva, and J. W. Larson (2001), An adaptive buddy check for observational quality control, *Q. J. R. Meteorol. Soc.*, *127*, 2451–2471, doi:10.1002/qj.49712757714.

Dubovik, O., T. Lapyonok, Y. J. Kaufman, M. Chin, P. Ginoux, R. A. Kahn, and A. Sinyuk (2008), Retrieving global aerosol sources from satellites using inverse modeling, *Atmos. Chem. Phys.*, *8*, 209–250, doi:10.5194/acp-8-209-2008.

Elbern, H., A. Strunk, H. Schmidt, and O. Talagrand (2007), Emission rate and chemical state estimation by 4-dimensional variational inversion, *Atmos. Chem. Phys.*, *7*, 3749–3769.

Fast, J. D., W. I. Gustafson Jr., R. C. Easter, R. A. Zaveri, J. C. Barnard, E. G. Chapman, G. A. Grell, and S. E. Peckham (2006), Evolution of ozone, particulates, and aerosol direct radiative forcing in the vicinity of Houston using a fully coupled meteorology-chemistry-aerosol model, *J. Geophys. Res.*, *111*, D21305, doi:10.1029/2005JD006721.

Gauthier, P., M. Tanguay, S. Laroche, S. Pellerin, and J. Morneau (2007), Extension of 3DVAR to 4DVAR: Implementation of 4DVAR at the Meteorological Service of Canada, *Mon. Weather Rev.*, *135*(6), 2339–2354.

Generoso, S., F.-M. Bréon, F. Chevallier, Y. Balkanski, M. Schulz, and I. Bey (2007), Assimilation of POLDER aerosol optical thickness into the LMDz-INCA model: Implications for the Arctic aerosol burden, *J. Geophys. Res.*, *112*, D02311, doi:10.1029/2005JD006954.

Ginoux, P., M. Chin, I. Tegen, J. M. Prospero, B. Holben, O. Dubovik, and S.-J. Lin (2001), Sources and distributions of dust aerosols simulated with the GOCART model, *J. Geophys. Res.*, *106*, 20,255–20,273, doi:10.1029/2000JD000053.

Green, D., G. Fuller, and B. Barratt (2001), Evaluation of TEOM^{TM} 'correction factors' for assessing the EU Stage 1 limit values for PM_{10}, *Atmos. Environ.*, *35*, 2589–2593.

Grell, G. A., S. E. Peckham, R. Schmitz, S. A. McKeen, G. Frost, W. C. Skamarock, and B. Eder (2005), Fully coupled "online" chemistry within the WRF model, *Atmos. Environ.*, *39*(37), 6957–6975.

Guenther, A., P. Zimmerman, and M. Wildermuth (1994), Natural volatile organic compound emission rate estimates for U.S. woodland landscapes, *Atmos. Environ.*, *28*(6), 1197–1210, doi:10.1016/1352-2310(94)90297-6.

Hakami, A., D. K. Henze, J. H. Seinfeld, T. Chai, Y. Tang, G. R. Carmichael, and A. Sandu (2005), Adjoint inverse modeling of black carbon during the Asian Pacific Regional Aerosol Characterization Experiment, *J. Geophys. Res.*, *110*, D14301, doi:10.1029/2004JD005671.

Henze, D. K., A. Hakami, and J. H. Seinfeld (2007), Development of the adjoint of GEOS-Chem, *Atmos. Chem. Phys.*, *7*, 2413–2433, doi:10.5194/acp-7-2413-2007.

Henze, D. K., J. H. Seinfeld, and D. T. Shindell (2009), Inverse modeling and mapping US air quality influences of inorganic $PM_{2.5}$ precursor emissions using the adjoint of GEOS-Chem, *Atmos. Chem. Phys.*, *9*, 5877–5903, doi:10.5194/acp-9-5877-2009.

Huang, J.-P., J. C. H. Fung, A. K. H. Lau, and Y. Qin (2005), Numerical simulation and process analysis of typhoon-related ozone episodes in Hong Kong, *J. Geophys. Res.*, *110*, D05301, doi:10.1029/2004JD004914.

Jang, J.-C., H. E. Jeffries, and S. Tonnesen (1995), Sensitivity of ozone to model grid resolution-II. Detailed processe analysis for ozone chemistry, *Atmos. Environ.*, *29*(21), 3101–3114.

Jeffries, H. E., and S. Tonnesen (1994), A comparison of two photochemical reaction mechanisms using mass balance and process analysis, *Atmos. Environ.*, *28*(18), 2991–3003, doi:10.1016/1352-2310(94)90345-X.

Jiang, G., B. Lamb, and H. Westberg (2003), Using back trajectories and process analysis to investigate photochemical ozone production in the Puget Sound region, *Atmos. Environ.*, *37*(11), 1489–1502, doi:10.1016/S1352-2310(02)01027-0.

Kahnert, M. (2008), Variational data analysis of aerosol species in a regional CTM: Background error covariance constraint and aerosol optical observation operators, *Tellus Ser. B*, *60*(5), 753–770, doi:10.1111/j.1600-0889.2008.00377.

Kalnay, E. (2010), Ensemble Kalman filter: Current status and potential, in *Data Assimilation: Making Sense of Observations*, edited by W. Lahoz, B. Khattatov, and R. Ménard, pp. 69–92, Springer, Berlin.

Kleist, D. T., D. F. Parrish, J. C. Derber, R. Treadon, W.-S. Wu, and S. Lord (2009), Introduction of the GSI into the NCEP Global Data Assimilation System, *Wea. Forecasting*, *24*(6), 1691–1705, doi:10.1175/2009WAF2222201.1.

Ku, B., and R. J. Park (2011), Inverse modeling analysis of soil dust sources over East Asia, *Atmos. Environ.*, *45*(32), 5903–5912, doi:10.1016/j.atmosenv.2011.06.078.

Lee, E.-H., J.-C. Ha, S.-S. Lee, and Y. Chun (2013), PM_{10} data assimilation over South Korea to Asian dust forecasting model with the optimal interpolation method, *Asia-Pacific J. Atmos. Sci.*, *49*(1), 73–85, doi:10.1007/s13143-013-0009-y.

Lin, C., Z. Wang, and J. Zhu (2008a), An ensemble Kalman filter for severe dust storm data assimilation over China, *Atmos. Chem. Phys.*, *8*, 2975–2983, doi:10.5194/acp-8-2975-2008.

Lin, C., J. Zhu, and Z. Wang (2008b), Model bias correction for dust storm forecast using ensemble Kalman filter, *J. Geophys. Res.*, *113*, D14306, doi:10.1029/2007JD009498.

Liu, S. C., et al. (1996), Model study of tropospheric trace species distributions during PEM-West A, *J. Geophys. Res.*, *101*, 2073–2085, doi:10.1029/95JD02277.

Liu, X.-H., Y. Zhang, J. Xing, Q. Zhang, K. Wang, D. G. Streets, C. Jang, W.-X. Wang, and J.-M. Hao (2010), Understanding of regional air pollution over China using CMAQ, part II. Process analysis and sensitivity of ozone and particulate matter to precursor emissions, *Atmos. Environ.*, *44*(30), 3719–3727.

Liu, Z., Q. Liu, H.-C. Lin, C. S. Schwartz, Y.-H. Lee, and T. Wang (2011), Three-dimensional variational assimilation of MODIS aerosol optical depth: Implementation and application to a dust storm over East Asia, *J. Geophys. Res.*, *116*, D23206, doi:10.1029/2011JD016159.

Lorenc, A. C., et al. (2000), The Met Office global three-dimensional variational data assimilation scheme, *Q. J. R. Meteorol. Soc.*, *126*(570), 2991–3012, doi: 10.1002/qj.49712657002.

McKeen, S. A., E.-Y. Hsie, M. Trainer, R. Tallamraju, and S. C. Liu (1991), A regional model study of the ozone budget in the eastern

United States, *J. Geophys. Res.*, *96*, 10,809–10,845, doi:10.1029/91JD00052.

McKeen, S., et al. (2007), Evaluation of several PM2.5 forecast models using data collected during the ICARTT/NEAQS 2004 field study, *J. Geophys. Res.*, *112*, D10S20, doi:10.1029/2006JD007608.

Misenis, C., and Y. Zhang (2010), An examination of sensitivity of WRF/Chem predictions to physical parameterizations, horizontal grid spacing, and nesting options, *Atmos. Res.*, *97*, 315–334, doi:10.1016/j.atmosres.2010.04.005.

Pagowski, M., and G. A. Grell (2012), Experiments with the assimilation of fine aerosols using an ensemble Kalman filter, *J. Geophys. Res.*, *117*, D21302, doi:10.1029/2012JD018333.

Pagowski, M., G. A. Grell, S. A. McKeen, S. E. Peckham, and D. Devenyi (2010), Three-dimensional variational data assimilation of ozone and fine particulate matter observations: Some results using the Weather Research and Forecasting—Chemistry model and Grid-point Statistical Interpolation, *Q. J. R. Meteorol. Soc.*, *136*(653), 2013–2024, doi:10.1002/qj.700.

Parrish, D. F., and J. C. Derber (1992), The National Meteorological Center's spectral statistical-interpolation analysis system, *Mon. Weather Rev.*, *120*(8), 1747–1763.

Rabier, F., A. McNally, E. Andersson, P. Courtier, P. Undén, J. Eyre, A. Hollingsworth, and F. Bouttier (1998), The ECMWF implementation of three-dimensional variational assimilation (3D-Var). II: Structure functions, *Q. J. R. Meteorol. Soc.*, *124*(550), 1809–1829, doi:10.1002/qj.49712455003.

Rabier, F., H. Jarvinen, E. Klinker, J.-F. Mahfouf, and A. Simmons (2000), The ECMWF operational implementation of four dimensional variational assimilation: Part I: Experimental results with simplified physics, *Q. J. R. Meteorol. Soc.*, *126*(564), 1143–1170.

Schroedter-Homscheidt, M., H. Elbern, and T. Holzer-Popp (2010), Observation operator for the assimilation of aerosol type resolving satellite measurements into a chemical transport model, *Atmos. Chem. Phys.*, *10*, 10,435–10,452, doi:10.5194/acp-10-10435-2010.

Schwartz, C. S., Z. Liu, H.-C. Lin, and S. A. McKeen (2012), Simultaneous three-dimensional variational assimilation of surface fine particulate matter and MODIS aerosol optical depth, *J. Geophys. Res.*, *117*, D13202, doi:10.1029/2011JD017383.

Simpson, D., A. Guenther, C. N. Hewitt, and R. Steinbrecher (1995), Biogenic emissions in Europe: 1. Estimates and uncertainties, *J. Geophys. Res.*, *100*, 22,875–22,890, doi:10.1029/95JD02368.

Streets, D. G., et al. (2003), An inventory of gaseous and primary aerosol emissions in Asia in the year 2000, *J. Geophys. Res.*, *108*(D21), 8809, doi:10.1029/2002JD003093.

Tombette, M., V. Mallet, and B. Sportisse (2009), PM_{10} data assimilation over Europe with the optimal interpolation method, *Atmos. Chem. Phys.*, *9*, 57–70, doi:10.5194/acp-9-57-2009.

Tonnesen, G. S. (1995), Development and application of a process analysis method for photochemical oxidant models, Ph.D. dissertation, Dep. of Environ. Eng., Univ. of N. C., Chapel Hill, May.

Tonnesen, G. S. and R. L. Dennis (2000a), Analysis of radical propagation efficiency to assess ozone sensitivity to hydrocarbons and NO_x: 1. Local indicators of instantaneous odd oxygen production sensitivity, *J. Geophys. Res.*, *105*, 9213–9225, doi:10.1029/1999JD900371.

Tonnesen, G. S., and R. L. Dennis (2000b), Analysis of radical propagation efficiency to assess ozone sensitivity to hydrocarbons and NO_x: 2. Long-lived species as indicators of ozone concentration sensitivity, *J. Geophys. Res.*, *105*, 9227–9241, doi:10.1029/1999JD900372.

Wang, J., U. S. Nair, and S. A. Christopher (2004), GOES 8 aerosol optical thickness assimilation in a mesoscale model: Online integration of aerosol radiative effects, *J. Geophys. Res.*, *109*, D23203, doi:10.1029/2004JD004827.

Wang, T., F. Jiang, J. Deng, Y. Shen, Q. Fu, Q. Wang, Y. Fu, J. Xu, and D. Zhang (2012), Urban air quality and regional haze weather forecast for Yangtze River Delta region, *Atmos. Environ.*, *58*, 70–83.

Wu, W.-S., R. J. Purser, and D. F. Parish (2002), Three-dimensional variational analyses with spatially inhomogeneous covariances, *Mon. Weather Rev.*, *130*(12), 2905–2916.

Yang, S., H. He, S. Lu, D. Chen, and J. Zhu (2008), Quantification of crop residue burning in the field and its influence on ambient air quality in Suqian, China, *Atmos. Environ.*, *42*(9), 1961–1969.

Yu, H., R. E. Dickinson, M. Chin, Y. J. Kaufman, B. N. Holben, I. V. Geogdzhayev, and M. I. Mishchenko (2003), Annual cycle of global distributions of aerosol optical depth from integration of MODIS retrievals and GOCART model simulations, *J. Geophys. Res.*, *108*(D3), 4128, doi:10.1029/2002JD002717.

Yumimoto, K., I. Uno, N. Sugimoto, A. Shimizu, and S. Satake (2007), Adjoint inverse modeling of dust emission and transport over East Asia, *Geophys. Res. Lett.*, *34*, L08806, doi:10.1029/2006GL028551.

Yumimoto, K., I. Uno, N. Sugimoto, A. Shimizu, Z. Liu, and D. M. Winker (2008a), Adjoint inversion modeling of Asian dust emission using lidar observations, *Atmos. Chem. Phys.*, *8*, 2869–2884, doi:10.5194/acp-8-2869-2008.

Yumimoto, K., I. Uno, N. Sugimoto, and A. Shimizu (2008b), MODIS AOT based inverse modeling for Asian dust, *SOLA*, *4*, 089−092, doi:10.2151/sola.2008-023.

Zhang, Y., P. Liu, B. Pun, and C. Seigneur (2006), A comprehensive performance evaluation of MM5-CMAQ for the summer 1999 Southern Oxidants Study episode—Part I: Evaluation protocols, databases, and meteorological predictions, *Atmos. Environ.*, *40*(26), 4825–4838, doi:10.1016/j.atmosenv.2005.12.043.

Zhang, J., J. S. Reid, D. L. Westphal, N. L. Baker, and E. J. Hyer (2008), A system for operational aerosol optical depth data assimilation over global oceans, *J. Geophys. Res.*, *113*, D10208, doi:10.1029/2007JD009065.

Zhang, Q., et al. (2009a), Asian emissions in 2006 for the NASA INTEX-B mission, *Atmos. Chem. Phys.*, *9*, 5131–5153, doi:10.5194/acp-9-5131-2009.

Zhang, Y., X.-Y. Wen, K. Wang, K. Vijayaraghavan, and M. Z. Jacobson (2009b), Probing into regional O_3 and particulate matter pollution in the United States: 2. An examination of formation mechanisms through a process analysis technique and sensitivity study, *J. Geophys. Res.*, *114*, D22305, doi:10.1029/2009JD011900.

Zhang, Y., X.-Y. Wen, and C. J. Jang (2010), Simulating chemistry-aerosol-cloud-radiation-climate feedbacks over the continental U.S. using the online-coupled Weather Research Forecasting Model with chemistry (WRF/Chem), *Atmos. Environ.*, *44*(29), 3568–3582.